



Numerical study of the primitive equations in the small viscosity regime

F. Gargano¹ · M. Sammartino² · V. Sciacca³

Received: 1 February 2018 / Revised: 29 May 2018 / Published online: 25 June 2018
© Università degli Studi di Napoli "Federico II" 2018

Abstract

In this paper we study the flow dynamics governed by the primitive equations in the small viscosity regime. We consider an initial setup consisting on two dipolar structures interacting with a no slip boundary at the bottom of the domain. The generated boundary layer is analyzed in terms of the complex singularities of the horizontal pressure gradient and of the vorticity generated at the boundary. The presence of complex singularities is correlated with the appearance of secondary recirculation regions. Two viscosity regimes, with different qualitative properties, can be distinguished in the flow dynamics.

Keywords Primitive equations · Zero viscosity limit · Singularity tracking methods

Mathematics Subject Classification 35Q35 · 76F40 · 35A21 · 65M70

1 Introduction

The primitive equations (PEs) are the fundamental equations governing the atmospheric and oceanic flows, see [43]. The system of the PEs is derived from the

In honor of Professor Tommaso Ruggeri, on the occasion of his 70th birthday..

✉ M. Sammartino
marcomarialuigi.sammartino@unipa.it

F. Gargano
francesco.gargano@unipa.it

V. Sciacca
vincenzo.sciacca@unipa.it

¹ Dipartimento di Energia, Ingegneria dell'Informazione e Modelli Matematici (DEIM),
Università degli Studi di Palermo, Palermo, Italy

² Dipartimento dell'Innovazione Industriale e Digitale (DIID), Università degli Studi di Palermo,
Palermo, Italy

³ Dipartimento di Matematica e Informatica, Università degli Studi di Palermo, Palermo, Italy

Boussinesq approximation assuming that the vertical length scale is small compared to the horizontal one. The relevant difference between the PEs and the usual Boussinesq equations lies in the fact that the momentum equation for the vertical velocity component is replaced by the hydrostatic balance for the pressure vertical gradient.

The mathematical analysis dealing with the PEs was essentially initiated in the fundamental works by Lions et al. [33–35], where the authors gave conditions for the existence of weak and strong solutions. These results were extended in [49] where the global existence of a weak solution was proved along with the local existence of a strong solution. In [10,30,31] the authors proved the existence of a unique global strong solution under different boundary conditions for the velocity components.

The analysis of the zero viscosity limit for the PEs is still challenging. In fact, when dealing with large scale motion of the ocean and considering the small scale over which viscosity acts, it is natural to neglect the viscous effect leading to the question whether the PEs converge to their inviscid counterpart, the hydrostatic Euler equation [36]. The complication arises because of the interaction with no slip boundaries and the consequent boundary layer formation. In [29] the authors investigated the vanishing viscosity problem for the PEs with no-slip boundary conditions both on the bottom and on the top, obtaining that, up to boundary layer correctors of order the square root of the viscosity, the PEs solutions converge to the hydrostatic Euler solution. The procedure required the expansion of the solution near the boundary with the inclusion of a corrector term to resolve the boundary layer and interpolate between the no slip condition and the tangential slip generated by the hydrostatic solution.

It is therefore clear that when solving the zero viscosity limit one needs also to face the mathematical and physical issues related to the hydrostatic Euler equation. In fact in [4,25,37] it was given evidence of a possible instability of the solution. Related to this instability is the possible blow-up of the solution. This was shown in [9], where the authors considered the 2D inviscid primitive equations and showed the finite time blow-up of the solution for a certain class of smooth initial data, and in [51] where the author considered the 3D case and gave evidence of the singularity formation by constructing self-similar solutions. An open problem is to prove whether the boundary layer corrector found in [29], develops or not singularity in finite time. In this case one could face a problem similar to the convergence of the Navier–Stokes solutions to the Prandtl solution, a long-standing problem which might be crucial to solve in order to ensure convergence of the Navier–Stokes solutions to the Euler solution outside the boundary layer. Recent results [23] have shown that the various viscous interactions developing in high Reynolds number Navier–Stokes solutions are due to the formation of complex singularities in the NS solutions.

Therefore one should expect that the convergence of the PEs solution to the hydrostatic Euler solution can be also addressed by investigating the presence of complex singularities in the PEs solution. The main aim of this paper to understand whether the PEs solutions display complex singularities, and how they move in the complex plane when viscosity becomes small. This will be accomplished by performing the complex singularity tracking for two relevant quantities obtained from the PEs solution, namely the vorticity generated at the bottom and the horizontal pressure gradient. This choice is mainly dictated by the fact that these quantities are commonly used in analyzing high Reynolds number Navier–Stokes solution see [21,23,24,40,41]. We shall see that

both quantities have complex singularities, and their presence is related to peculiar physical events manifesting in the flow evolution.

The rest of the paper is organized as follows. In Sect. 2 we shall introduce the primitive equations and we shall state the physical problem. In Sect. 3 we shall describe the flow evolution obtained from the numerical solution of the PEs, and we shall mainly analyze the boundary layer evolution in terms of energy and enstrophy of the flow. In Sect. 4 we shall briefly review the singularity tracking method, and we shall explain the numerical procedure used to determine the positions and the character of the singularities. In Sects. 4.1 and 4.2 we shall present the results of the singularity tracking applied to the pressure gradient and to the vorticity generated at the bottom of the domain. Finally in Sect. 5 we shall draw some conclusions.

2 Statement of the problem

The primitive equations for a velocity field $\mathbf{u}(x, y) = (u(x, y), v(x, y))$ driven by the pressure $p(x, y)$, where $(x, y) \in D = \mathbb{T} \times [-h, 0]$, with $h > 0$, read as

$$\partial_t u + u\partial_x u + v\partial_y u + \partial_x p = \nu (\partial_{xx} u + \partial_{yy} u), \tag{1}$$

$$\partial_x u + \partial_y v = 0, \tag{2}$$

$$\partial_y p = 0, \tag{3}$$

$$\gamma_D^- u = \gamma_D^- v = 0, \tag{4}$$

$$\gamma_N^+ u = \gamma_D^+ v = 0, \tag{5}$$

$$u(x, y, t = 0) = u_0(x, y), \tag{6}$$

where we suppose that the velocity components and the pressure are periodic in $x \in \mathbb{T}$ and

$$\gamma_D^- f(x, y) = f(x, y = -h), \tag{7}$$

$$\gamma_D^+ f(x, y) = f(x, y = 0), \tag{8}$$

$$\gamma_N^+ f(x, y) = \partial_y f(x, y)|_{y=0}. \tag{9}$$

In the above system, (1) is the equation for the horizontal velocity component u where ν is the kinematic viscosity of the flow, (2) is the incompressibility condition, (3) is the condition ensuring that the pressure is constant along the vertical direction, (4) and (5) are the boundary conditions for the velocity components on the bottom and on the top, and (6) is the initial condition.

To retrieve the pressure gradient in (1) we need to recover the pressure p . This is accomplished by deriving (1) with respect to the horizontal x variable and then averaging along the vertical direction y , obtaining the following equation for p :

$$\partial_{xx} p = \frac{1}{h} \left(\int_{-h}^0 \partial_{xx} u^2 d\tilde{y} - \nu [\partial_{xy} u]_{y=-h}^{y=0} \right), \tag{10}$$

The normal velocity is computed from (2)

$$v(x, y) = - \int_{-h}^y \partial_x u(x, \tilde{y}) d\tilde{y}, \tag{11}$$

and in view of (5), we have that

$$v(x, 0) = - \int_{-h}^0 \partial_x u(x, \tilde{y}) d\tilde{y} = 0. \tag{12}$$

Condition (12) is guaranteed for all time if the horizontal and vertical components u and v of the velocity are respectively even and odd along the extended vertical domain $[-h, h]$. The boundary conditions (4) and (5) and the Eqs. (1) and (2) imply that u and v preserve these symmetries during the dynamics as long as it is satisfied initially. The choice of using the homogeneous Neumann BC for u at the top reflects the fact that free slip is the physical condition commonly used for atmospheric and oceanic flows. To ensure these requests, we put $\mathbb{T} = [0, 2\pi]$, and consider the following initial condition for u :

$$u_0(x, y) = \left[e^{-\left(\frac{y-y_0}{\sigma}\right)^2} - e^{-\left(\frac{y-(-h-y_0)}{\sigma}\right)^2} \right] e^{-\left(\frac{x-\pi}{\sigma}\right)^2},$$

which satisfies (4) and (5) for sufficiently small σ , and represents a pair of dipolar structures centered in $(\pi, (-h - y_0))$ and (π, y_0) , see Fig. 1a.

2.1 The numerical scheme

The whole system is solved using a spectral numerical scheme based on a fully Fourier spectral discretization for the x variable and on a collocation Chebyshev discretization for the y variable. In particular, due to the periodicity of the problem, the spatial discretization is based on following expressions for the main variables:

$$u(x, y, t) \approx \sum_{k=-M_x/2}^{k=M_x/2} u_k(y, t) e^{ikx}, \quad v(x, y, t) \approx \sum_{k=-M_x/2}^{k=M_x/2} v_k(y, t) e^{ikx}, \tag{13}$$

$$p(x, t) \approx \sum_{k=-M_x/2}^{k=M_x/2} p_k(t) e^{ikx}, \tag{14}$$

where $x_k = 2\pi k/M_x$, $k = 0, \dots, M_x$ are the $M_x + 1$ grid points in the horizontal domain. The grid points in the vertical domain are $y_j = \frac{w_j h - h}{2}$, $j = 0, \dots, M_y$, where $w_j = \cos(\pi(j/M_y - 1))$ are the collocation Gauss–Lobatto points in $[-1, 1]$.

Time-integration is based on a two-stage Runge–Kutta algorithm where the discretization of the linear part is of the Crank–Nicolson type (see [44]). In particular ,

each mode k satisfies the following sets of equations in y :

$$u_k^1 = u_k^n + \Delta t \left[N(u_k^n, v_k^n, p_k^n) + \frac{1}{2}L(u_k^n) + \frac{1}{2}L(u_k^1) \right], \tag{15}$$

$$u_k^{n+1} = u_k^n + \frac{\Delta t}{2} \left[N(u_k^n, v_k^n, p_k^n) + N(u_k^1, v_k^1, p_k^1) + L(u_k^n) + L(u_k^{n+1}) \right] \tag{16}$$

where the superscript indicates the n th time step, and Δt is the time step. In (15) and (16) the linear part is defined as

$$L(u_k) = \nu \left(-k^2 u_k + \frac{4}{h^2} \mathbb{D}^2 u_k \right),$$

where \mathbb{D} is the y -derivative matrix operator. Entries of \mathbb{D} are generally defined for functions approximated in the Gauss–Lobatto nodes, and are easily found in the literature of the spectral methods [3,8,44]. The nonlinear part is defined as

$$N(u_k, v_k, p_k) = -(u * u_x)_k - \left(\frac{2}{h} v * \mathbb{D}u \right)_k + ikp_k(t),$$

where by $*$ we have denoted the (pseudo)spectral multiplication in the x variable, which is treated with the usual 3/2-method to handle aliasing effects, see [8].

Equations (15) and (16) can be recast in matrix form $\mathcal{A}U_k^{1,n+1} = F^{1,n+1}$, where $U_k^{1,n+1} = (u_k^{1,n+1}(y_0), \dots, u_k^{1,n+1}(y_{M_y}))^T$, $\mathcal{A} = (1 + \nu k^2)\mathcal{I} - \nu \frac{4}{h^2} \mathbb{D}^2$ with \mathcal{I} the identity matrix of order $(M_y + 1) \times (M_y + 1)$. The vector $F^{1,n+1}$ contains in the first and last entry $\gamma_D^- u$ and $\gamma_N^+ u$, and in the interior entries the terms of (15) and (16) treated explicitly. To take into account the boundary conditions (4) and (5) for the velocity component u , the first and the last row of \mathcal{A} are expressed according the well known collocation formulas found for instance in [44].

In the above terms, the vertical velocity component v is retrieved from (11) through the spectral Chebyshev integration along the vertical variable (see [50]), while each mode p_k is retrieved from the elliptic problem (10) according to the following straightforward spectral integration:

$$p_k(t) = - \frac{\left(\int_{-h}^0 -k^2(u * u)_k dy + ik\nu \left[\frac{2}{h} \mathbb{D}u_k \right]_{y=-h}^{y=0} \right)}{2k^2h}, \quad k \neq 0 \tag{17}$$

$$p_0(t) = 0. \tag{18}$$

We observe that the pressure is independent on the vertical variable, and therefore it is expressed only in terms of Fourier modes. Hence we do not have any spurious mode arising when we solve spectrally the elliptic problem (10) (see [2,8] for detailed discussions on this numerical issue in the general case in which the pressure is y -dependent).

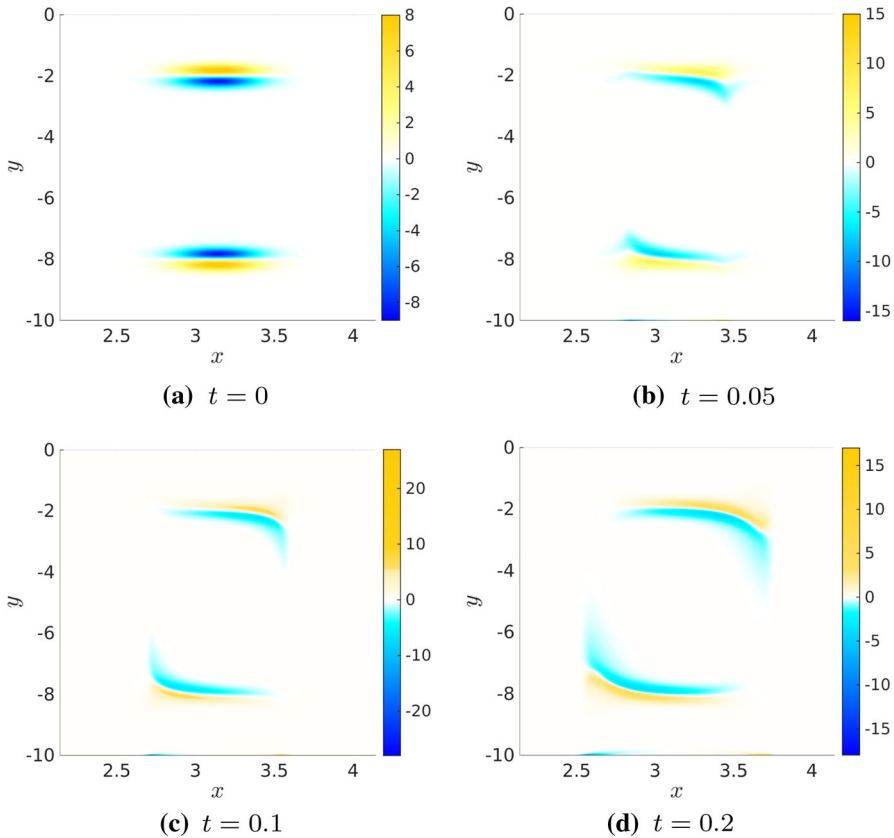


Fig. 1 Vorticity ω at various time for $\nu = 0.01$. The initial vorticity consists in a pair of dipolar structures centred in $y = -8$ and $y = -2$. At subsequent times vorticity is generated at the bottom, due to the no-slip boundary condition for the horizontal velocity component

3 Physics of the flow

In this section, we shall describe the main physical events characterizing the early flow evolution governed by the PEs, where we have fixed $h = 10$, $y_0 = -2$, $\sigma = 1/4$ in the initial condition (13). The physical events arising during the flow evolution will be described for two different viscosity regimes, the moderate–high regime $\nu \geq 0.01$, and the low regime $\nu < 0.01$. We shall mainly describe the flow in term of vorticity evolution $\omega(x, y, t) = -\partial_y u(x, y, t)$, vorticity generated at the bottom $\omega_b(x, t) = \omega(x, y = -h, t)$, pressure gradient $\partial_x p$, energy $E = \frac{1}{2} \|u\|_{L^2(D)}^2$ and the enstrophy $\mathcal{E} = \|\omega\|_{L^2(D)}^2$. All the above quantities are relevant and have been used to describe the various interactions leading to the onset of turbulence especially in boundary layer flows (see results on high Reynolds number Navier–Stokes solutions [13,21,23,27]).

The moderate–high viscosity regime, represented by the case $\nu = 0.01$, is strongly affected by the high dissipative effects induced by the viscosity. Vorticity evolution is shown in Figs. 1 and 2b at different times. The pair of dipolar structures centered in

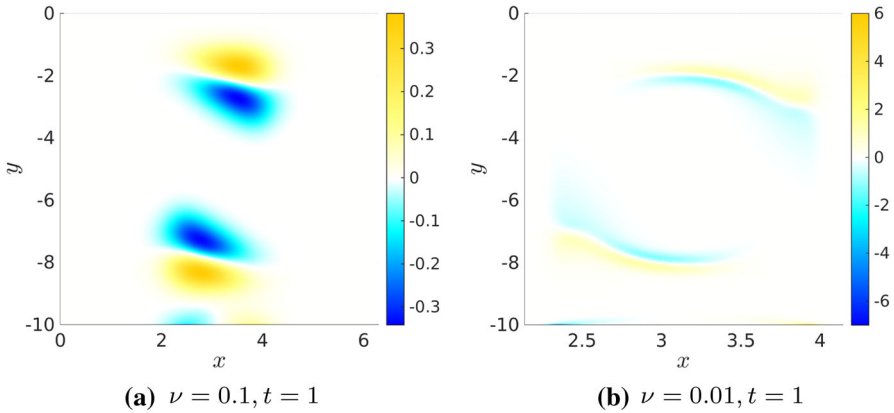


Fig. 2 Vorticity ω at $t = 1$ for $\nu = 0.1$ and $\nu = 0.01$

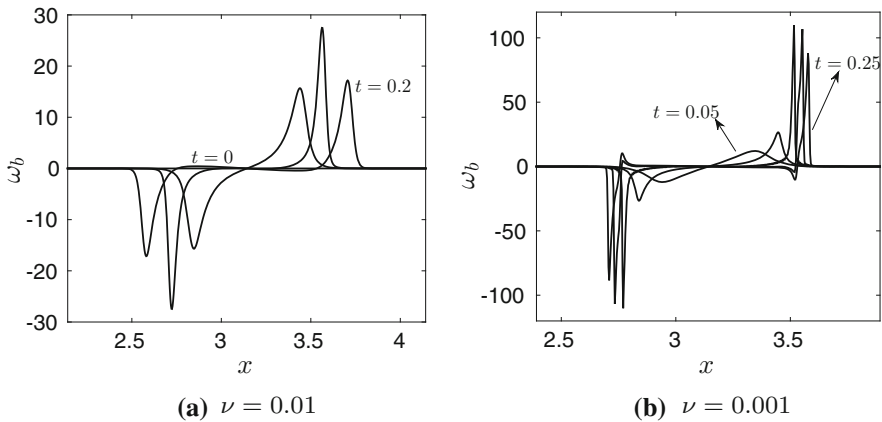


Fig. 3 Vorticity ω_b produced at the bottom $y = -h$ at various time (increments of $\Delta t = 0.05$) for $\nu = 0.01$, representing the moderate–high viscosity regime, and $\nu = 0.001$, representing the low viscosity regime

$y = -8, -2$ are rapidly stretched along the horizontal direction. During the clockwise rotation of the dipolar structures, a boundary layer attached to the bottom forms due to the no-slip boundary condition, and two recirculation eddies having opposite rotation are generated. They are barely visible at $t = 0.2$ in Fig. 1d, while the vorticity ω_b generated at the bottom is shown at different times in Fig. 3a (the eddies generated at the bottom are better visible in Fig. 2 for $\nu = 0.1$ and $\nu = 0.01$ at time $t = 1$). One can see that $\omega_b(x) \leq 0$ for $x \lesssim \pi$ while $\omega_b(x) \geq 0$ for $x \gtrsim \pi$. The different sign is justified by the sign variation in $x \approx \pi$ observed in $\partial_x p$ (see Fig. 4b at $t = 0$), which accelerates flow particles for $x \lesssim \pi$ whereas decelerates them for $x \gtrsim \pi$. As time passes, the eddies thicken essentially along the horizontal direction, and spikes in ω_b and $\partial_x p$ form at $t \approx 0.1$ (see Figs. 3a, 4b). After $t \approx 0.1$, ω_b and $\partial_x p$ begin to weaken, and the eddies generated at the bottom continue to have small vertical extension and low strength. The weak vorticity production and the weakness of the eddies generated at the bottom can also be inferred by enstrophy time evolution (Fig. 5a) which, despite

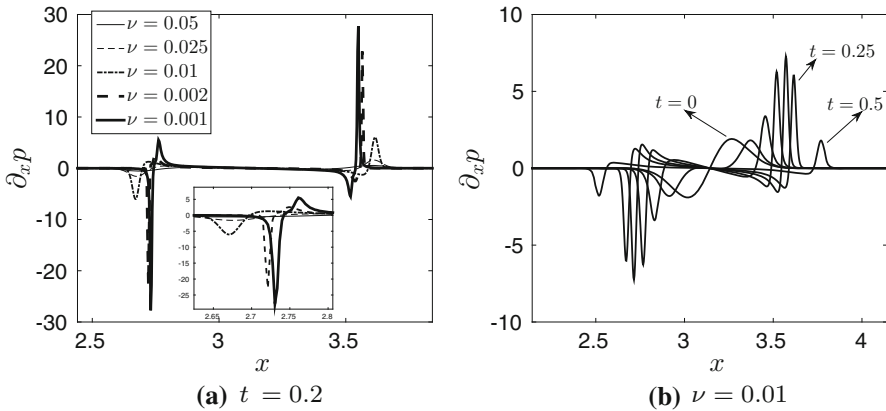


Fig. 4 **a** The horizontal pressure gradient $\partial_x p$ for various ν at $t = 0.2$, with a magnification in the inset, **b** time evolution of $\partial_x p$ for $\nu = 0.01$ from $t = 0$ up to $t = 0.25$ (time increments of $\Delta t = 0.05$) and at $t = 0.5$

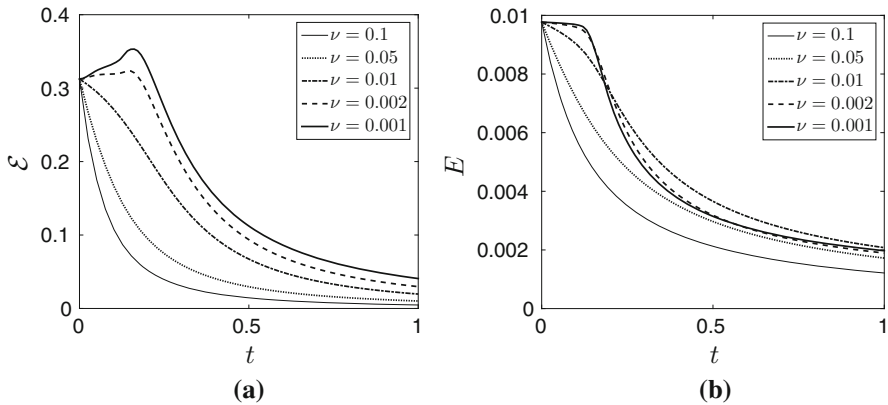


Fig. 5 **a** Time evolution of the Entropy \mathcal{E} for various ν , from $t = 0$ up to $t = 1$. Only for the low viscosity regime ($\nu = 0.002, 0.001$) the vorticity production at the bottom leads to the entropy growth, **b** time evolution of the Energy E for various ν , from $t = 0$ up to $t = 1$

the vorticity generated at the bottom, is always decreasing for all time. Subsequent flow evolution shows no relevant physical phenomena, and due to the high dissipative effects the flow tends to the rest with almost vanishing energy (see Fig. 5b).

The low viscosity regime, represented by the case $\nu = 0.001$, shows some physical phenomena already observed in moderate–high regime. In fact a boundary layer consisting in two eddies forms at the bottom, although the lower viscosity effects allow for a higher production than in the moderate–high regime case. Secondary recirculation regions form in time, and they can be deduced by the change in the sign of ω_b observed for $t \approx 0.2$ at $x \approx 2.76, 3.52$ in Fig. 3b. The secondary recirculation regions formation are mainly due to the strong variations observed in the pressure gradient $\partial_x p$. In fact in correspondence of the points where secondary recirculation regions form, the pressure gradient becomes adverse (the change of sign is visible in Fig. 4a) with respect to the flow direction between the primary recirculation region and the

bottom. This variation in the pressure gradient sign is concentrated in a very narrow horizontal zone and, depending on the sign, induces a strong acceleration/deceleration which eases the formation of a new recirculation regions.

The relevant difference with respect to the moderate–high regime lies in the \mathcal{E} growth observed as ν decreases (Fig. 5a), mainly due to the high vorticity production at the bottom. \mathcal{E} is a main responsible of dissipation of energy (see energy evolution in Fig. 5b). In fact, standard computations allow to write the energy equation $\frac{dE(t)}{dt} = -\nu \left(\mathcal{E}(t) + \|\partial_x u(t)\|_{L^2(D)}^2 \right)$, from which one can observe how \mathcal{E} induces a decay in the energy E . After $t \geq 0.15$, when the secondary recirculation region is forming, the enstrophy begins to decrease, and no other peak is observed. The enstrophy growth has been observed in our simulations only for $\nu \leq 0.002$. The enstrophy growth in the low viscosity regime is typical of the flows characterized by the formation of the boundary layer, and has been observed for a wide class of high Reynolds number boundary layer flows: for the rectilinear vortex case [21,24], for the impulsively started disk [23], and for the dipole-vortex flow [14,15].

4 Singularity tracking

One of the main goal of our investigation is to analyze the singular character of the solution of the PEs in the zero viscosity limit. This is accomplished by performing the singularity tracking in the complex plane. Singularity tracking has been widely used to analyze loss of analyticity in many equations arising in fluid dynamics: Euler flow [5,6,12,18,38,42], boundary layer flow [16,17,20,23,24], Camassa-Holm equations [17], KdV equation [19,26], vortex-sheet flow [1,7,22,28,47,48].

Here we apply the singularity tracking to the vorticity generated at the boundary ω_b and the horizontal pressure gradient $\partial_x p$ obtained from the numerical solution of the PEs. The choice of tracking the singularities of $\omega_b, \partial_x p$ relies on the fact that in many low viscosity/high Reynolds number flows, some of the relevant physical phenomena of the boundary layer have been successfully described and understood in terms of the character of the vorticity generated on a rigid boundary and of the pressure gradient (see in particular [23] and the analysis done on the viscous-inviscid interactions ruling the zero viscosity limit in boundary layer flow).

The singularity tracking is based on the asymptotic properties of the spectrum of an analytic function. In particular, suppose that $u(z)$ is a real function having a complex singularity in $z^* = x^* + i\delta$ and that $u(z) \approx (z - z^*)^{\alpha+i\tau}$. Using a steepest descent argument one can show that the asymptotic (in k) behaviour of the spectrum u_k of $u(z)$ is the following (see [11]):

$$u_k \approx C|k|^{-(1+\alpha)} e^{-\delta|k|} \sin(kx^* + \tau \log(k) + \phi). \tag{19}$$

The estimation of δ and x^* gives the complex location of the singularity z^* , while determining the rate of algebraic decay $1 + \alpha$ and the rate of oscillatory behaviour τ allows to classify the character of the singularity. C and ϕ are constants related to the strength and phase of the singularity. To apply the singularity tracking method

to $\omega_b, \partial_x p$, we actually consider that they are even function, so that it is enough to apply (19) to the Fourier expansions $\omega_b(x, t) = \sum_{k \geq 0} \omega_k(t) \sin kx$, $\partial_x p(x, t) = \sum_{k \geq 0} p_k(t) \sin kx$, with $x \in [0, \pi]$. Hence, for symmetry reasons, for any singularity placed $z_1^* = x^* + i\delta$ there will be another singularity placed in $z_2^* = 2\pi - x^* + i\delta$ having the same character of z_1^* .

To find, at each time, the parameters in (19), we consider that they should be in principle independent on the wavenumber k , although in practice they are k dependent and are better determined in specific band of k . Hence, following [1,22], we impose that (19) holds point-wise for each k , and for each k we equate six consecutive modes $u_{k-5}, u_{k-4}, u_{k-3}, u_{k-2}, u_{k-1}, u_k$ to the form in (19), obtaining a nonlinear system for the parameters $C, \alpha, \delta, x^*, \tau, \phi$ whose solution returns the k -dependent values of the parameters. Specific band of k in which the parameters $C, \alpha, \delta, x^*, \tau, \phi$ are actually k independent are typically the first 80 wavenumbers although the amplitude of this band depends also on how many modes are affected by the roundoff errors of the machine. Hence at each time we assume as values for the various parameters in (19) those obtained in the range of wavenumbers where they are k independent.

4.1 Singularity of $\partial_x p$

We first discuss the results for $\partial_x p$, and in particular how the viscosity ν influences the singularity analysis. In Fig. 6a–c we show the results coming from the numerical fitting of (19) for $k \leq 80$ and for various ν at $t = 0.2$, when the secondary recirculation regions have been formed for all ν considered.

We first notice that in all cases and for each time, the evaluation of the character of the complex singularities of $\partial_x p$ has always returned a real value, due to vanishing of the complex part τ of the character. We observe from Fig. 6a that the character $\alpha_{\partial_x p}$ is in each case negative, compatible with a blow up of the complexification of $\partial_x p$ close $x_{\partial_x p}^* + i\delta_{\partial_x p}$ and the consequent eruptive behaviour observed in Fig. 4a for the pressure gradient. Although $\alpha_{\partial_x p}$ is shown only for $t = 0.2$, also for subsequent times its value remains essentially the same, showing some instability only when the singularity is quite far from the real domain, because in (19) the exponential decay $e^{-\delta_{\partial_x p} k}$ dominates over the algebraic decay given by $k^{-(1+\alpha_{\partial_x p})}$.

The effect of decreasing ν strongly influences the character $\alpha_{\partial_x p}$, especially when passing from the moderate–high viscosity regime to the low regime. In fact, for $\nu \leq 0.002$, the character $\alpha_{\partial_x p}$ abruptly decreases with ν , expressing the fact that the complex singularity has a stronger character. The real part $x_{\partial_x p}^*$ of the complex singularity location well agrees with the position in which $\partial_x p$ has an eruptive behaviour (see Fig. 4a). However the most striking effect of a decreasing viscosity shows on the distance of the singularity from the real domain: from Fig. 6c we can observe that it diminishes for decreasing ν , meaning that for $\nu \rightarrow 0$ the pressure gradient becomes less regular, a condition which is compatible with the abrupt eruptive behaviour which characterizes $\partial_x p$ for small ν values.

In Fig. 6d we show the tracking of the complex singularity $x_{\partial_x p}^* + i\delta_{\partial_x p}$ in the complex plane for various ν from $t = 0.05$ up to $t = 0.5$. At each time the singularity is closer to the real domain as ν decreases, and in all cases the singularity, after

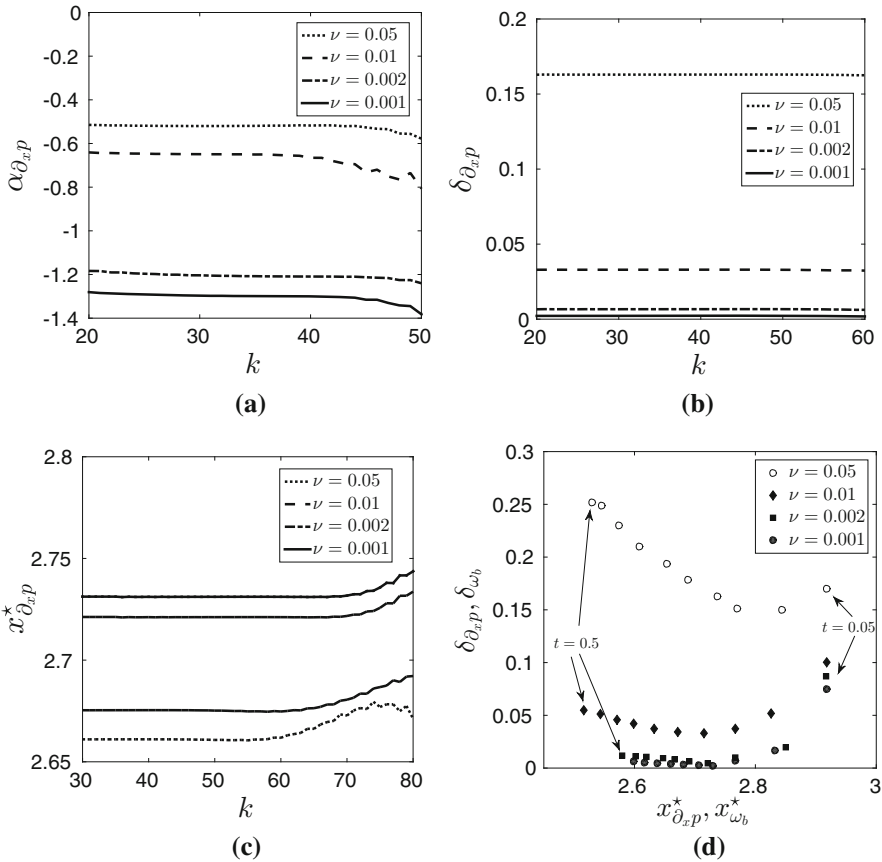
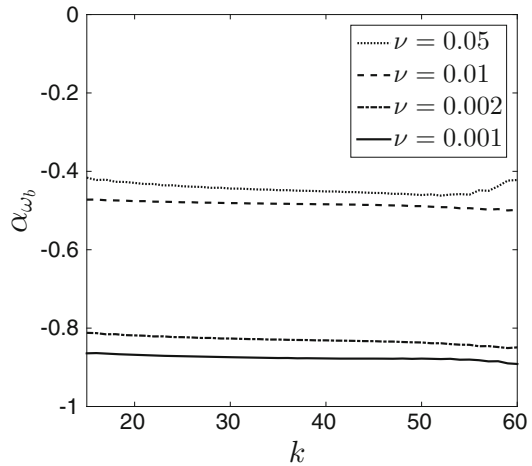


Fig. 6 Results of the numerical fitting of (19) applied to the horizontal pressure gradient $\partial_x p$ at $t = 0.2$ for various ν . **a** Fitting of the real character $\alpha_{\partial_x p}$, **b** fitting of the width of analyticity $\delta_{\partial_x p}$, **c** fitting of the real part $x_{\partial_x p}^*$ of the position of the singularity, **d** tracking in the complex plane of the singularities $x_{\partial_x p}^* + i\delta_{\partial_x p}$ and $x_{\omega_b}^* + i\delta_{\omega_b}$ of $\partial_x p$ and ω_b for various ν and from $t = 0.05$ (right) up to $t = 0.5$ (left), time increments of $\Delta t = 0.05$. The two singularities share the same positions in the complex plane. For symmetry reasons there are also the singularities $2\pi - x_{\partial_x p}^* + i\delta_{\partial_x p}$ and $2\pi - x_{\omega_b}^* + i\delta_{\omega_b}$

reaching a minimal distance from the real domain, begins to travel away from the real axis. This expresses the fact that, after the time in which this distance is minimal, $\partial_x p$ acquires a smoother behavior and the amplitude of its peaks diminishes as shown for instance in Fig. 4b for the case $\nu = 0.01$. In all cases the time of minimal distance of the singularity from the real domain is essentially coinciding with the time when the secondary recirculation region forms in the boundary layer. This is reminiscent of what we have observed in the previous section, i.e. a smoother flow evolution after the formation of the secondary recirculation region.

Fig. 7 Numerical evaluation trough (19) of the real character α_{ω_b} of the main singularity of ω_b at $t = 0.2$ for various ν



4.2 Singularity of ω_b

The singularity tracking method applied to ω_b has returned results that share similarities with the same analysis performed for $\partial_x p$. From the evolution of ω_b visible in Fig. 3a, b one can easily observe that the eruptive behaviour, especially visible for $\nu = 0.001$, forms in the same positions where $\partial_x p$ has its main peaks (see Fig. 4a and the case $\nu = 0.001$). Therefore one can expect that this reflects the presence of singularities also in ω_b , having the same position of the singularities of $\partial_x p$ in complex plane. This is actually what we have obtained from the numerical evaluation of $x_{\omega_b}^* + ix_{\omega_b}^\delta$ (and of the symmetric singularity $2\pi - x_{\omega_b}^* + ix_{\omega_b}^\delta$): the tracking of the singularity $x_{\omega_b}^* + ix_{\omega_b}^\delta$ in the complex plane is essentially the same of $x_{\partial_x p}^* + ix_{\partial_x p}^\delta$, and it is shown in Fig. 6d.

Regarding the character of the singularity, also in this case the imaginary part is almost negligible, and α_{ω_b} obtained from the fitting of the form (19) is shown in Fig. 7 for various ν at $t = 0.2$. The obtained values are almost k -independent in the first 80 wavenumber, with values in each case negative. This reflects that the complexified ω_b blows up close to the singularity, and ω_b consequently shows the eruptive behaviour visible in Fig. 3b for $\nu = 0.001$. Also for ω_b we have obtained that α_{ω_b} remains almost the same for subsequent time. With respect to $\partial_x p$, ω_b has a slightly more regular behavior, due to the fact that for all ν we have obtained $\alpha_{\omega_b} \geq \alpha_{\partial_x p}$.

5 Conclusions

We have computed the solutions of the two-dimensional primitive equations in moderate–low viscosity regime. Imposing the no-slip boundary condition at the bottom of the domain leads to a boundary layer development, with high vorticity production and formation of high horizontal gradient in the pressure. In the low viscosity regime, typically $\nu \leq 0.002$, small scale phenomena, supporting the formation of secondary

recirculation regions in the boundary layer, have been observed. These phenomena are related to the high vorticity production at the boundary, an event leading also to the global growth of the enstrophy in the early flow evolution. For moderate–high viscosity, $\nu \geq 0.01$, the evolution is characterized by a weak vorticity production, with no growth of the enstrophy in time.

The two viscosity regimes have been also analyzed in terms of complex singularities of the horizontal pressure gradient $\partial_x p$ and the vorticity ω_b generated at the bottom. The main result is that both quantities have complex singularities which are closer to the real domain as ν decreases. All the singularities tracked show negative characters, stronger in the low viscosity regime. This reflects the eruptive behavior observed in $\partial_x p$ and ω_b . In all cases the singularities reach, at a specific time, a minimal distance from the real domain and, after this event, they begin to depart from the real domain. This expresses that the width of the analyticity of the solution becomes larger, and the overall flow evolution becomes smoother; it is easy to guess that, asymptotically, the flow reaches a rest state, an event which can be predicted by the decay of the energy.

The numerical solutions we have obtained share some similarities with the high Reynolds number Navier–Stokes solutions analyzed in different configurations, see [15,21,23,39–41]. In fact, high Reynolds number flows present the typical small scale phenomena here observed in the PEs solutions, as well as the presence of complex singularities in the solution which are precursor of the interactions between the boundary layer and inviscid outer flow. In [23] it was reported a comparison between the complex singularities of the Navier–Stokes solution and the Prandtl singularity, showing how NS solutions have a much richer singular structure which, apparently, cannot be approximated by the Prandtl singularity. We plan to perform a similar investigation for the PEs. Moreover, it would be interesting to study the asymptotic behavior of the solutions of the PEs using the Fourier Splitting technique, see [45], in analogy to what recently proposed in [46] for the shallow water model with varying bottom topography proposed in [32]. This is a work in progress that will appear elsewhere.

Acknowledgements The authors thank an anonymous referee for suggestions and comments that helped improving the presentation of the paper. The work of MS and VS was partially supported by GNFM–INdAM. The work of FG was partially supported by the GNFM–INdAM Progetto Giovani Grant.

References

1. Baker, G., Caffisch, R., Siegel, M.: Singularity formation during Rayleigh–Taylor instability. *J. Fluid Mech.* **252**, 51–75 (1993)
2. Bernardi, C., Maday, Y.: Uniform inf-sup conditions for the spectral discretization of the Stokes problem. *Math. Models Methods Appl. Sci.* **9**(3), 395–414 (1999)
3. Boyd, J.: *Chebyshev and Fourier Spectral Methods*, p. 11501. DOVER Publications, Mineola (2000)
4. Brenier, Y.: Homogeneous hydrostatic flows with convex velocity profiles. *Nonlinearity* **12**(3), 495–512 (1999)
5. Caffisch, R.: Singularity formation for complex solutions of the 3D incompressible Euler equations. *Physica D* **67**(1–3), 1–18 (1993)
6. Caffisch, R., Gargano, F., Sammartino, M., Sciacca, V.: Complex singularities and PDEs. *Riv. Mat. Univ. Parma* **6**(1), 69–133 (2015)
7. Caffisch, R., Gargano, F., Sammartino, M., Sciacca, V.: Regularized Euler- α motion of an infinite array of vortex sheets. *Boll. Unione Mat. Ital.* **10**(1), 113–141 (2017)

8. Canuto, C., Hussaini, M., Quarteroni, A., Zang, T.A.: Spectral Methods in Fluid Dynamics. Computational Physics. Springer, Berlin (1988)
9. Cao, C., Ibrahim, S., Nakanishi, K., Titi, E.: Finite-time blowup for the inviscid primitive equations of oceanic and atmospheric dynamics. *Commun. Math. Phys.* **337**(2), 473–482 (2015)
10. Cao, C., Titi, E.: Global well-posedness of the three-dimensional viscous primitive equations of large scale ocean and atmosphere dynamics. *Ann. Math.* **166**(1), 245–267 (2007)
11. Carrier, G., Krook, M., Pearson, C.: Functions of a Complex Variable: Theory and Technique. McGraw-Hill, New York (1966)
12. Cichowlas, C., Brachet, M.E.: Evolution of complex singularities in Kida–Pelz and Taylor–Green inviscid flows. *Fluid Dyn. Res.* **36**(4–6), 239–248 (2005)
13. Clercx, H., van Heijst, G.: Dissipation of coherent structures in confined two-dimensional turbulence. *Phys. Fluids* **29**(11), 111,103 (2017)
14. Clercx, H., Bruneau, C.H.: The normal and oblique collision of a dipole with a no-slip boundary. *Comput. Fluids* **35**(3), 245–279 (2006)
15. Clercx, H., van Heijst, G.: Dissipation of kinetic energy in two-dimensional bounded flows. *Phys. Rev. E* **65**(6), 066,305 (2002)
16. Cowley, S.: Computer extension and analytic continuation of Blasius’ expansion for impulsively flow past a circular cylinder. *J. Fluid Mech.* **135**, 389–405 (1983)
17. Della Rocca, G., Lombardo, M., Sammartino, M., Sciacca, V.: Singularity tracking for Camassa–Holm and Prandtl’s equations. *Appl. Numer. Math.* **56**(8), 1108–1122 (2006)
18. Frisch, U., Matsumoto, T., Bec, J.: Singularities of Euler flow? Not out of the blue!. *J. Stat. Phys.* **113**(5), 761–781 (2003)
19. Gargano, F., Ponetti, G., Sammartino, M., Sciacca, V.: Complex singularities in KdV solutions. *Ric. Mat.* **65**(2), 479–490 (2016)
20. Gargano, F., Sammartino, M., Sciacca, V.: Singularity formation for Prandtl’s equations. *Physica D* **238**(19), 1975–1991 (2009)
21. Gargano, F., Sammartino, M., Sciacca, V.: High Reynolds number Navier–Stokes solutions and boundary layer separation induced by a rectilinear vortex. *Comput. Fluids* **52**, 73–91 (2011)
22. Gargano, F., Sammartino, M., Sciacca, V.: Fluid mechanics: singular behavior of a vortex layer in the zero thickness limit. *Rend. Lincei Math. Appl.* **28**(3), 553–572 (2017)
23. Gargano, F., Sammartino, M., Sciacca, V., Cassel, K.: Analysis of complex singularities in high-Reynolds-number Navier–Stokes solutions. *J. Fluid Mech.* **747**, 381–421 (2014)
24. Gargano, F., Sammartino, M., Sciacca, V., Cassel, K.: Viscous-inviscid interactions in a boundary-layer flow induced by a vortex array. *Acta Appl. Math.* **132**, 295–305 (2014)
25. Grenier, E.: On the derivation of homogeneous hydrostatic equations. *Math. Model. Numer. Anal.* **33**(5), 965–970 (1999)
26. Klein, C., Roidot, K.: Numerical study of shock formation in the dispersionless Kadomtsev–Petviashvili equation and dispersive regularizations. *Physica D* **265**, 1–25 (2013)
27. Kramer, W., Clercx, H., van Heijst, G.: Vorticity dynamics of a dipole colliding with a no-slip wall. *Phys. Fluids* **19**(12), 126,603 (2007)
28. Krasny, R.: A study of singularity formation in a vortex sheet by the point-vortex approximation. *J. Fluid Mech.* **167**, 65–93 (1986)
29. Kukavica, I., Lombardo, M., Sammartino, M.: Zero viscosity limit for analytic solutions of the primitive equations. *Arch. Rational Mech. Anal.* **222**(1), 15–45 (2016)
30. Kukavica, I., Ziane, M.: On the regularity of the primitive equations of the ocean. *Nonlinearity* **20**(12), 2739–2753 (2007)
31. Kukavica, I., Ziane, M.: The regularity of solutions of the primitive equations of the ocean in space dimension three. *C. R. Math.* **345**(5), 257–260 (2007)
32. Levermore, C., Sammartino, M.: A shallow water model with eddy viscosity for basins with varying bottom topography. *Nonlinearity* **14**(6), 1493–1515 (2001)
33. Lions, J.L., Temam, R., Wang, S.: On the equations of the large-scale ocean. *Nonlinearity* **5**(5), 1007–1053 (1992)
34. Lions, J.L., Temam, R., Wang, S.: Mathematical theory for the coupled atmosphere–ocean models. *J. Math. Pures Appl.* **74**(2), 105–163 (1995)
35. Lions, J.L., Temam, R., Wang, S.: A simple global model for the general circulation of the atmosphere. *Commun. Pure Appl. Math.* **50**(8), 707–752 (1997)

36. Lions, P.L.: *Mathematical topics in fluid mechanics, vol. 1. Oxford Lecture Series in Mathematics and its Applications, vol. 3. Incompressible models.* The Clarendon Press, Oxford University Press, New York (1996)
37. Masmoudi, N., Wong, T.K.: On the H^s theory of hydrostatic Euler equations. *Arch. Rational Mech. Anal.* **204**(1), 231–271 (2012)
38. Matsumoto, T., Bec, J., Frisch, U.: The analytic structure of 2D Euler flow at short times. *Fluid Dyn. Res.* **36**(4–6), 221–237 (2005)
39. Nguyen Van Yen, R., Farge, M., Schneider, K.: Energy dissipating structures produced by walls in two-dimensional flows at vanishing viscosity. *Phys. Rev. Lett.* **106**, 184502 (2011)
40. Obabko, A., Cassel, K.: Navier-Stokes solutions of unsteady separation induced by a vortex. *J. Fluid Mech.* **465**, 99–130 (2002)
41. Obabko, A., Cassel, K.: On the ejection-induced instability in Navier–Stokes solutions of unsteady separation. *Philos. Trans. A Math. Phys. Eng. Sci.* **363**(1830), 1189–1198 (2005)
42. Pauls, W., Matsumoto, T., Frisch, U., Bec, J.: Nature of complex singularities for the 2D Euler equation. *Physica D* **219**(1), 40–59 (2006)
43. Pedlosky, J.: *Geophysical Fluid Dynamics.* Springer, New York (1979)
44. Peyret, R.: *Spectral Methods for Incompressible Viscous Flow.* Springer, New York (2002)
45. Schonbek, M.: l^2 decay for weak solutions of the Navier–Stokes equations. *Arch. Rational Mech. Anal.* **88**(3), 209–222 (1985)
46. Sciacca, V., Schonbek, M., Sammartino, M.: Long time behavior for a dissipative shallow water model. *Ann. Inst. H. Poincaré Anal* **34**(3), 731–757 (2017)
47. Shelley, M.: A study of singularity formation in vortex-sheet motion by a spectrally accurate vortex method. *J. Fluid. Mech.* **244**, 493–526 (1992)
48. Sohn, S.I.: Singularity formation and nonlinear evolution of a viscous vortex sheet model. *Phys. Fluids* **25**(1), 014,106 (2013)
49. Temam, R., Ziane, M.: *Some Mathematical Problems in Geophysical Fluid Dynamics.* Handbook of Mathematical Fluid Dynamics, vol. III. North-Holland, Amsterdam (2004)
50. Trefethen, L.: *Spectral Methods in MATLAB. Environments, and Tools.* Society for Industrial and Applied Mathematics, Software (2000)
51. Zheng, L., Wang, S.: Finite-time blowup for the 3-D primitive equations of oceanic and atmospheric dynamics. *Appl. Math. Lett.* **76**, 117–122 (2018)